Biophysical Journal, Volume 99

Supporting Material

Title: A simulation study of cellular hypertrophy and connexin lateralization in cardiac tissue

Authors: Thomas Seidel, Aida Salameh, and Stefan Dhein

SUPPORTING MATERIAL

A simulation study of cellular hypertrophy and connexin lateralization in cardiac tissue

Thomas Seidel, Aida Salameh, and Stefan Dhein

INDEX

DETAILED METHODS

Mapping and immunostaining of atrial human tissue

We obtained tissue samples (10mm×10mm) from 14 patients suffering from mitral valve disease (both male and female, aged 40-75 years) either with atrial fibrillation (n=7) or without (n=7), i.e., sinus rhythm, undergoing cardiac surgery. The patients did not receive beta-blockers or any anti-arrhythmic drugs. Written informed consent was obtained from all patients in this study. The institutional Ethical Committee approved the study. The investigation conforms to the principles outlined in the Declaration of Helsinki. Atrial tissue from all patients was obtained from the right atrial free wall during cardiac surgery, placed in cold Tyrode solution and was transported directly to the lab. For mapping the tissue was fixed, superfused with Tyrode solution (Na^+ 161.02; K^+ 5.36; Ca^{2+} 1.8, Mg^{2+} 1.05; Cl^- 147.86; HCO_3^- 23.8; PO_4^{3-} 0.42 and glucose 11.1mmol l^{-1}; equilibrated with 95% O_2 and 5% CO_2 (pH=7.4)) and 64 electrodes (rectangular, 1mm spacing) were placed on the top of the tissue. Centrally two electrodes were placed for pacing using rectangular pulses of 1Hz, 0.6mA, and 1ms duration. The resulting activation wavefront was analyzed with respect to the fiber orientation. For analysis we used our mapping system HAL4, determined the activation times as t(dV/dt_{min}) and constructed 0.25ms isochrones from which θ_L and θ_T were calculated as described previously (1,2). Formalin fixed, paraffin embedded tissue sections of 5µm thickness were immunostained for Cx43 as described (3) using rabbit anti-Cx43 antibodies (Sigma, St. Louis, USA) diluted 1:2000 with Dako Cytomation Antibodies Diluent (Dako Cytomation, Glostrup, Danmark) at 4°C overnight and FITC-labelled polyclonal swine anti-rabbit secondary antibodies diluted 1:32 in Tris-buffered saline for 1h at 4°C. The specificity was controlled by omitting the primary antibodies. The sections were investigated at 1,000× magnification using a commercial image analysis system (Zeiss Vision) and Zeiss Axiolab fluorescence microscope (Zeiss, Jena, Germany). The slices were discarded when the imaging plane was not parallel to the long axis of the fibers. For evaluation, the longitudinal cell axis, the left and the right cell pole was determined. We measured the length of the plasma membrane of each cell at the cell pole and in the middle as well as the length of the immunofluorescence-positive membrane in each part of the cell. From these data we calculated the ratio between positively stained membrane length and plasma membrane length for the cell pole and the lateral side of the cell as described (3).

Figure S1

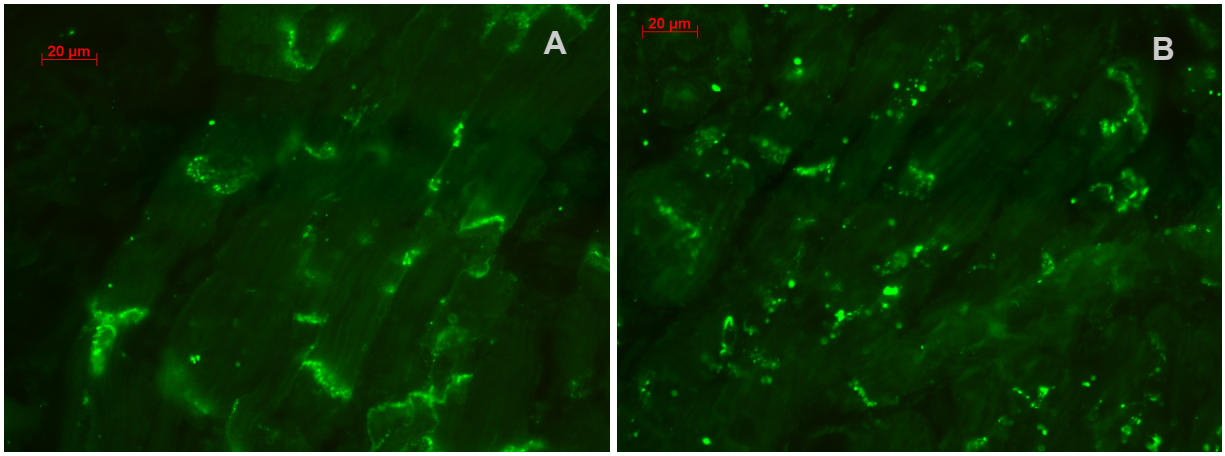

FIGURE S1 Examples of original immunohistology for Cx43 (*green*) in human left atrium (free wall). Samples were obtained from patients with sinus rhythm (*A*) or with atrial fibrillation (*B*).

The single cell / membrane model

For each membrane segment, total transmembrane current, I_m in pA/µm², was calculated using the Priebe- Beuckelmann model (4) of human cardiomyocytes, which is based on the dynamic Luo-Rudy-II model (5).
Specific membrane capacity, C_m, was 0.01pF/µm². Thus, the voltage change per time is

$$\frac{\partial \varphi}{\partial t} = \frac{1}{C_m} I_m$$

I_m is the sum of all ionic currents across the cell membrane:

$$I_m = I_{Na} + I_{Ca} + I_{to} + I_{K1} + I_{Kr} + I_{Ks} + I_{Na,b} + I_{Ca,b} + I_{NaK} + I_{NaCa}$$

Extracellular space is assumed to be grounded. Thus, transmembrane voltage is identical with intracellular voltage.
Equations for time- and voltage-dependent currents are adopted from the Priebe-Beuckelmann model. Gated channels are described by Hodgkin-Huxley (6) type formalism:

$$\frac{\partial y}{\partial t} = \alpha_y - y(\alpha_y + \beta_y)$$

where y stands for the gating variable. α_y and β_y depend on the transmembrane voltage φ.

Ionic concentrations
The model is dynamic, i.e. each ionic current I_s changes ionic concentrations in the extracellular and intracellular space:

$$\frac{\partial [s]_i}{\partial t} = - \frac{I_s A_m}{F z_s V_{myo}} \quad , \quad \frac{\partial [s]_o}{\partial t} = \frac{I_s A_m}{F z_s V_{cleft}}$$

where $[s]_i$ and $[s]_o$ is the concentration of ion species s in intracellular and extracellular space, respectively, A_m denotes membrane area, V_{myo} the myoplasmatic volume and V_{cleft} the extracellular volume. However, since in this study only a very short period of time was simulated (less than 500ms), changes in ionic concentrations were marginal. Initial ionic concentrations which were chosen for simulations can be retrieved from Table S1.

Ion	Domain	Concentration
Ca^{++}	intracellular	0.3µmol/l
Ca^{++}	extracellular	2.0mmol/l
Ca^{++}	NSR	1.5mmol/l
Ca^{++}	JSR	1.5mmol/l
Na^{+}	intracellular	10.0mmol/l
Na^{+}	extracellular	145.0mmol/l
K^{+}	intracellular	140.0mmol/l
K^{+}	extracellular	5.4mmol/l

TABLE S1 Initial ionic concentrations.

Spatial and temporal integration in 2D

The continuity equation expressing charge conservation in 2D is given by

$$\frac{\partial \rho}{\partial t} = -\left(\frac{\partial \vec{J}}{\partial x} + \frac{\partial \vec{J}}{\partial y} \right) \tag{1}$$

where ρ is the charge density in C/m³, t is the time, $\vec{J}$ is the current density in A/m² and x and y are the two spatial dimensions.
Ohm's law is given by

$$\vec{J} = \vec{E}\sigma \tag{2}$$

where $\vec{E}$ is the electrical field in V/m and σ is the specific conductivity in S/m.
$\vec{E}$ is calculated by

$$\vec{E} = -\nabla \Phi \tag{3}$$

where Φ is the electrical potential in V and ∇ is the Nabla vector, i.e., the gradient.
If σ is constant, Eq. 1, Eq. 2 and Eq. 3 result in:

$$\frac{\partial \rho}{\partial t} = \sigma \left(\frac{\partial^2 \Phi}{\partial x^2} + \frac{\partial^2 \Phi}{\partial y^2} \right) \tag{4}$$

Division by the specific membrane capacity, C_m, the ratio of capacitive to geometric membrane area R_{CG}, and the ratio of geometrical membrane area to volume, R_{AV}, leads to:

$$\frac{\partial \Phi}{\partial t} = \frac{\sigma}{C_m R_{CG} R_{AV}} \left(\frac{\partial^2 \Phi}{\partial x^2} + \frac{\partial^2 \Phi}{\partial y^2} \right) \tag{5}$$

where $D = \sigma / \left(C_m R_{CG} R_{AV} \right)$ is the diffusion coefficient.
Replacing Φ by the transmembrane voltage φ, we get the common partial differential equation for two dimensions:

$$\frac{\partial \varphi}{\partial t} = D \left(\frac{\partial^2 \varphi}{\partial x^2} + \frac{\partial^2 \varphi}{\partial y^2} \right) \tag{6}$$

It should be noted that Eq. 4, Eq. 5 and Eq. 6 are only valid if D is a constant. Generally, σ is a tensor depending on space and time. This results in a more complex equation:

$$\frac{\partial \varphi}{\partial t} = D^* \left(\frac{\partial}{\partial x} \left(\sigma_{x,y} \frac{\partial \varphi}{\partial x} \right) + \frac{\partial}{\partial y} \left(\sigma_{x,y} \frac{\partial \varphi}{\partial y} \right) \right) \tag{6*}$$

Note that we used Eq. 6* in order to allow the simulation of anisotropic, inhomogeneous cardiac tissue with σ being a function of space and time. D^* ($=C_m R_{CG} R_{AV}$), which depends on cell geometry, was assumed to be constant over space and time in each simulation. But it altered with the chosen

cell geometry (see Table 1 in the main article).
However, for better understanding and clearness, only the discretization of Eq. 6 is shown below.

The rectangular domain of interest, $\Omega = [0, X; 0, Y]$, is divided into $(N+1)\times(M+1)$ rectangles of $\Delta x \times \Delta y$ in size, where $\Delta x = \Delta y$ and $N = \frac{X}{\Delta x} - 1, M = \frac{Y}{\Delta y} - 1$. The index for x is i with i=0..N, the index for y is j with j=0..M. Each grid point (i,j) represents a cell segment.
A compact finite difference scheme with non-flux boundary conditions (7) for solving the right-hand side of Eq. 6 is as follows:

$$\frac{\partial^2 \varphi_{i-1,j}}{\partial x^2} + 10\frac{\partial^2 \varphi_{i,j}}{\partial x^2} + \frac{\partial^2 \varphi_{i+1,j}}{\partial x^2} = \frac{12\varphi_{i-1,j} - 24\varphi_{i,j} + 12\varphi_{i+1,j}}{(\Delta x)^2} \tag{7}$$

$$2\frac{\partial^2 \varphi_{0,j}}{\partial x^2} + \frac{\partial^2 \varphi_{1,j}}{\partial x^2} = \frac{-6\varphi_{0,j} + 6\varphi_{1,j}}{(\Delta x)^2} \tag{8}$$

$$2\frac{\partial^2 \varphi_{N,j}}{\partial x^2} + \frac{\partial^2 \varphi_{N-1,j}}{\partial x^2} = \frac{-6\varphi_{N,j} + 6\varphi_{N-1,j}}{(\Delta x)^2} \tag{9}$$

Equation 7 is for interior points, Eq. 8 and Eq. 9 are for boundary points. The error in x- and y-direction is of 4th order at interior points and of 2nd order at boundary points. For the y-direction, the equations are analog.
For discretization of the left-hand side of Eq. 6, a time step of $\Delta t = 0.001\text{ms}$ was used. Smaller time steps were tested. They increased the temporal resolution but did not change the results. The fully implicit scheme of Eq. 6 is as follows:

$$\frac{\varphi^{t+\Delta t} - \varphi^t}{\Delta t} = D\left(\frac{\partial^2 \varphi^{t+\Delta t}}{\partial x^2} + \frac{\partial^2 \varphi^{t+\Delta t}}{\partial y^2}\right) \tag{10}$$

Equation 7, Eq. 8, Eq. 9 and Eq. 10 can be written in matrix form and were solved by common linear matrix algorithms.

Simulating 2D myocardium

Based on the mathematical principles described above, a computer simulation model of a two-dimensional (2D) cellular monolayer of ventricular cardiomyocytes lying in the *x*-*y*-plane was created. Each grid point of the 2D mesh represented a cell segment with a size of Δx in *x*-direction and of Δy in *y*-direction. If not otherwise specified, $\Delta x = \Delta y = 10\mu m$ was used. Cell segments were interconnected via intracellular resistivities if belonging to the same cell and via junctional resistances if belonging to adjacent cells. This approach is similar to the discontinuous model of Spach et al. (8) and can be recognized as an extension of the one-dimensional Shaw-Rudy model (9) to two dimensions. Specific membrane capacity, C_m, had a constant value of $0.01 pF/\mu m^2$ and was always multiplied by the ratio of capacitive to geometric membrane area, $R_{CG}=2$. Cells were assumed to be cylindrical. Thus, total membrane capacity per cell, C_{cell}, was calculated by $C_{cell} = C_m \times R_{CG} \times A_m$, with $A_m = 2\pi r(l+r)$ being the geometrical membrane area of a cell with the radius *r* and the length *l*. Each segment had a capacity of $C_{segment} = C_m \times R_{CG} \times V_{segment} \times R_{AV}$ with $V_{segment}$ being the volume per segment. R_{AV} of a cylinder is calculated by $R_{AV} = A/V = (2\pi rl + 2\pi r^2)/(\pi r^2 l) = 2/r + 2/l$. Geometrical parameters are shown in Table 1 in the main article.

Cytoplasmic resistivity was set to 1.5Ωm (8-11), corresponding to 0.67S/m, extracellular space was assumed to be grounded. Polar and lateral junctional resistances were varied between 0.08MΩ and 1000MΩ, translating into gap junction conductances (g_{GJ}) between 13µS and 1nS, respectively. Total g_{GJ} per cell, was defined as the gap junction conductance sum of all membrane segments belonging to one cell. In control cells, polar g_{GJ} was 3.7µS, lateral g_{GJ} was 2.6µS. These values were chosen because dual-cell patch clamp experiments demonstrated that the ratio of polar-to-lateral g_{GJ} is ~1 (12,13) and conduction velocities similar to or slightly higher than those measured in healthy myocardium (11,13-15) were obtained (θ_L=0.59m/s and θ_T=0.16m/s; θ_L/θ_T=3.6). Electrophysiological parameters are shown in Table 2 in the main article. Conductance values defined as 100% of coupling were higher than those mostly measured in dual-cell patch clamp experiments (13,16-18), where intercellular conductances mainly range between 50nS and 500nS. However, they are in agreement with gap junction conductances that were necessary in other computer simulations to obtain conduction velocities of approx. 50cm/s in longitudinal direction: Shaw et al. (9) obtained a θ_L of 52cm/s with 2.5µs, Spach et al. (8) obtained a θ_L of 48cm/s with 0.8µs. Using a polar g_{GJ} of 2.5µS we obtained exactly the same value (52cm/s) as Shaw et al (9).

A possible explanation for the apparent discrepancy between models and real tissue may be an overestimation of myocardial conduction velocity: End-to-end conductances of 350nS still resulted in conduction velocities around 0.4m/s, which is not unrealistic. It should also be noted that in a mono-domain model as used in this study, the extracellular space does not contribute to impulse propagation, i.e., in a bi-domain model same velocities might be obtained at lower g_{GJ}. Furthermore, it may be possible that isolated cell pairs which are used for dual-cell voltage clamp experiments are partially uncoupled, i.e., show a lower g_{GJ} than they would have in intact tissue.

Cell arrangement

In cardiac tissue, cells are usually not regularly aligned (Fig. S2 *A*) but rather arranged brick-like (Fig. S2 *B* and *C*), with overlapping cell ends. Furthermore, cells are often branched near their poles, presenting jutting ends. It has been shown that brick-like arrangement allows lateral gap junctions to contribute to longitudinal propagation via zigzag conduction patterns and that jutting ends can also modulate transverse and longitudinal conduction velocity (19,20). However, since the objective of this study was to simulate cellular hypertrophy, irregular cell forms as they are essential for jutting ends, would have required further assumptions and might have interfered with increased cell width. Therefore, only regular cell forms were simulated. In order to verify the influence of different degrees of overlapping (Fig. S2), two different degrees were simulated and compared with respect to electrophysiological behavior. Note that in all other simulations, the grade of overlapping as shown in Fig. S2 *B* was used, because it corresponds best to histological findings.

Analytical data

Activation time

Activation time was defined as the point in time when the m-gate of the fast sodium channel had reached a value ≥ 0.5 and was recorded for each cell segment, allowing the calculation of conduction velocities and activation patterns both on tissue and cellular level. Other authors use $\varphi \geq$ -40mV as activation threshold. However, we could find that our definition corresponds better to the time of maximum upstroke velocity of the transmembrane potential and that conduction velocities were independent of the activation criterion. A cell was fully activated when all its segments were activated.

Conduction velocity

Conduction velocity (θ) between two cells was calculated dividing the spatial distance by the activation time difference. Transverse θ, θ_T, was measured between membrane segments at y-position 80 and 160. Longitudinal θ, θ_L, was measured between membrane segments at x-position 100 and 260.

Charge and axial currents

In- and outflowing intra- and intercellular currents (I_{in} and I_{out}) were recorded for each cell segment. The net current ($I_{net} = I_{in} - I_{out}$) provides information about the charge a segment is accumulating from or emitting to other cells and cell segments. The time integral of I_{net} was interpreted as the depolarizing charge, Q_{net}, a cell segment had accumulated ($Q_{net} > 0$) or emitted ($Q_{net} < 0$) with respect to the tissue. Note that this charge does not involve the charge which is gained or lost by transmembrane currents (I_{ion}). It is therefore an indicator of current sources ($Q_{net} < 0$) and current sinks ($Q_{net} > 0$) with respect to the tissue. The interval of integration always began at t=0ms (time of stimulation) and ended at a point in time which was of interest. See also Figure S5 for explanation. The model was verified summing up the charges from intercellular and from transmembrane currents over the interval of a whole action potential. The sum was zero, indicating that the law of charge conservation was not violated.

Intracellular and junctional delay

The activation time difference between two adjacent cell segments belonging to different cells was defined as junctional (GJ) delay. The activation time difference between the last activated and the first activated cell segment within one cell was defined as intracellular delay.

Conduction block

If after having applied the stimulation current and before all cells were activated the transmembrane voltage of all cells had fallen below -60mV, conduction block was manifested.

Minimum stimulation current

The minimum magnitude of the stimulation current (I_{stim}) which was sufficient to induce stable impulse propagation, was determined by holding the stimulation time (t_{stim}) and the stimulation area (A_{stim}) constant while I_{stim} was gradually increased starting from zero. Interestingly, minimum I_{stim} was almost equal to the "charge wave" traveling in front of the activation wave front (see Fig. S7).

Limitations of the model

Calculation of membrane-area-to-volume ratio

For a cylindrical cell with the radius r and the length l, we get:

$$R_{\mathrm{AV}} = \frac{A}{V} = \frac{2\pi rl + 2\pi r^2}{\pi r^2 l} = \frac{2}{r} + \frac{2}{l}$$

This is the average for a whole cell. But within a cell, near cell poles and lateral borders, R_{AV} could be higher, whereas it could be lower in the middle of the cell. However, it is not clear if the whole volume of a cell equally contributes to electrical conductance or if there are areas with lower or higher conductivity. So it is difficult to assess whether the decrease in R_{AV} when cell radius increases, is linear or not. Therefore, it seemed reasonable to assume a linear relation and to assume that each segment of a cell has the same R_{AV} value. Multiplying R_{AV} with the specific membrane capacity C_m (and its correction factor R_{CG}=2) and the intracellular resistivity ρ_{ic} results in the intracellular diffusion coefficient D:

$$D_{ic} = 1/(R_{AV} \times C_m \times R_{CG} \times \rho_{ic})$$

Since $l > r$, R_{AV} is mainly determined by the cell radius, i.e., D_{ic} is approx. proportional to r. Accordingly, a twofold increase in r leads to an approx. twofold increase in D_{ic}.

Transmembrane currents

In normal and in hypertrophied cells, all transmembrane ionic channels were assumed to have the same density per membrane area, i.e., specific maximum conductivities were unchanged. Also current channel kinetics were assumed to be unchanged. It is known that in hypertrophied hearts and in heart failure ionic currents and ionic concentrations can be altered. Especially the fast sodium current (I_{Na}) and the L-type calcium current (I_{Ca}) would have great effect on impulse propagation. Yet, there is data suggesting that I_{Ca} remains unchanged (21), while data regarding I_{Na} are controversial (22,23). Mere hypertrophy would rather decrease the densities of these currents leading to decreased conduction velocities and earlier conduction block, which could potentiate the effects found in this study. Changes in repolarizing currents, e.g., I_{K1}, were less important for this study, because repolarization was not analyzed. But the aim was to analyze the effects of connexin lateralization and of cellular hypertrophy, so transmembrane current densities were held constant.

Simulation of gap junctions and connexin lateralization

Active behavior of gap junctions was not incorporated for several reasons. It is known that gap junction conductance can be modulated metabolically, especially by the pH-value and by intracellular Ca^{++}. Furthermore, many studies show a voltage-dependent gating behavior of gap junction channels, especially when high potential gradients (usually >50mV) are applied over time intervals of >1000ms. But since the simulated conditions didn't include metabolic alterations or ischemia and since the time interval was in the range of between 100 and 500ms, it was decided to model gap junctions as passive ohmic resistances. Simulating connexin lateralization, functionality of lateral gap junctions was assumed, i.e., histological data showing an increase of connexin43-positive membrane area was directly translated into a corresponding increase in gap junction conductivity because there are some studies giving evidence for functionality (13,24). In order to take into account the possibility that lateral GJ conductance remains unchanged, we also simulated altered GJ distribution with constant conductance.

2D versus 3D

In order to reduce the model to 2D, neighboring cells in z-direction were assumed to be equipotential (no-flow conditions). In 3D, GJ lateralization and hypertrophy would not only affect currents in y- but also in z-direction. Thus, in 3D tissue, the effects of hypertrophy and connexin lateralization which were observed in 2D would probably be more distinct. Increased lateral currents would not only flow in y-direction but also in z-direction and might lead to conduction block very early if g_{Na} is reduced and to a strongly reduced conduction velocity under conditions of cellular uncoupling.

E.g., Fast et al. (25), demonstrated that the critical strand diameter at tissue expansion decreased more than twofold in 3D as compared to 2D. However, all results obtained from 2D simulations would have the same tendency in 3D, only the magnitude could be different. The aim of this study was to get an mechanistic insight into effects of the varied parameters and therefore a computationally efficient 2D model was chosen.

Inhomogeneities

In real myocardium, especially in diseased myocardium, there would probably be variations not only in cardiomyocytes but as well in the intercellular matrix and in the number of fibroblasts (1). We decided to incorporate no inhomogeneities and no fibroblasts in order to avoid interferences. Within the simulated tissue, all cells were assumed to be equal, i.e., no variability regarding cell size, arrangement or transmembrane currents was simulated. Taking variability and fibrosis into account could be the aim of a further study.

Mono-domain versus bi-domain

In this study, the extracellular space was assumed to be grounded, which would correspond to a monolayer of cells within an extracellular bath. It has been recently shown that the extracellular space may attenuate effects of alterations in gap junction conductances and distribution (26). Extracellular space might also contribute to intercellular currents, leading to lower g_{GJ} at a given conduction velocity. But there is not much experimental data on this issue and it seems probable that basic effects and mechanisms would remain the same.

Cx43-immunostaining and mapping of human atrial cells

As already described in the methods section of the main article, immunostaining does not provide a good quantitative measurement of the gap junction number. Furthermore, it doesn't give any functional data. We therefore measured longitudinal and transverse conduction velocities, showing that the "increase" of lateral Cx43 was accompanied by an increase in lateral velocity. This gives evidence of functionality, but still isn't a proof. There might be other alterations leading to increased lateral velocity, e.g., changes in transmembrane currents. In further studies, it would be necessary to combine immunostaining with double-cell patch clamp experiments in order to obtain GJ conductances.

ADDITIONAL RESULTS

Figure S2

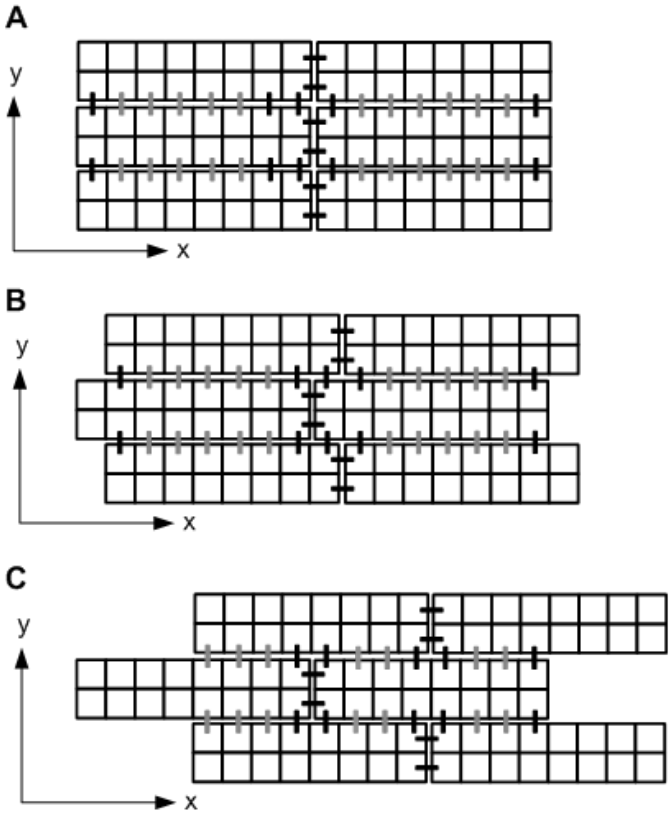

FIGURE S2 Different degrees of cellular overlapping: No overlapping (*A*), minimum degree of overlapping (*B*) and maximum degree of overlapping (*C*). Black horizontal bars indicate polar gap junctions (GJ), black and gray vertical bars indicate transverse GJ. GJ lateralization is characterized by a uniform lateral GJ distribution, i.e., gray and black vertical bars indicate the same conductance. In normal cells, GJ indicated by gray bars cover only 10% of lateral g_{GJ}, i.e., 90% of lateral g_{GJ} is provided by lateral GJ near the cell poles (black vertical bars).

If there is no overlapping (*A*), lateral GJ conductance cannot contribute to longitudinal propagation on a cellular level because upstream and downstream cells are only interconnected via polar GJ. If lateral conductance is concentrated near the poles, a small overlap (*B*) is enough to let almost 50% of the lateral GJ conductance contribute to longitudinal propagation, which has stabilizing effects on longitudinal conduction velocity (see Figs. 6 and 7 in the main article). But if lateral conductance is distributed uniformly over the lateral cell side, only a small percentage of the lateral conductance can contribute to longitudinal propagation. A small overlap seems to be the most realistic assumption, since it corresponds best to histological findings, and was therefore used in all simulations. However, if an overlap of 50% of the cell length (*C*) was simulated, there was no difference between normal and uniform lateral GJ distribution because in both cases 50% of the lateral GJ could contribute to longitudinal propagation.

Figure S3

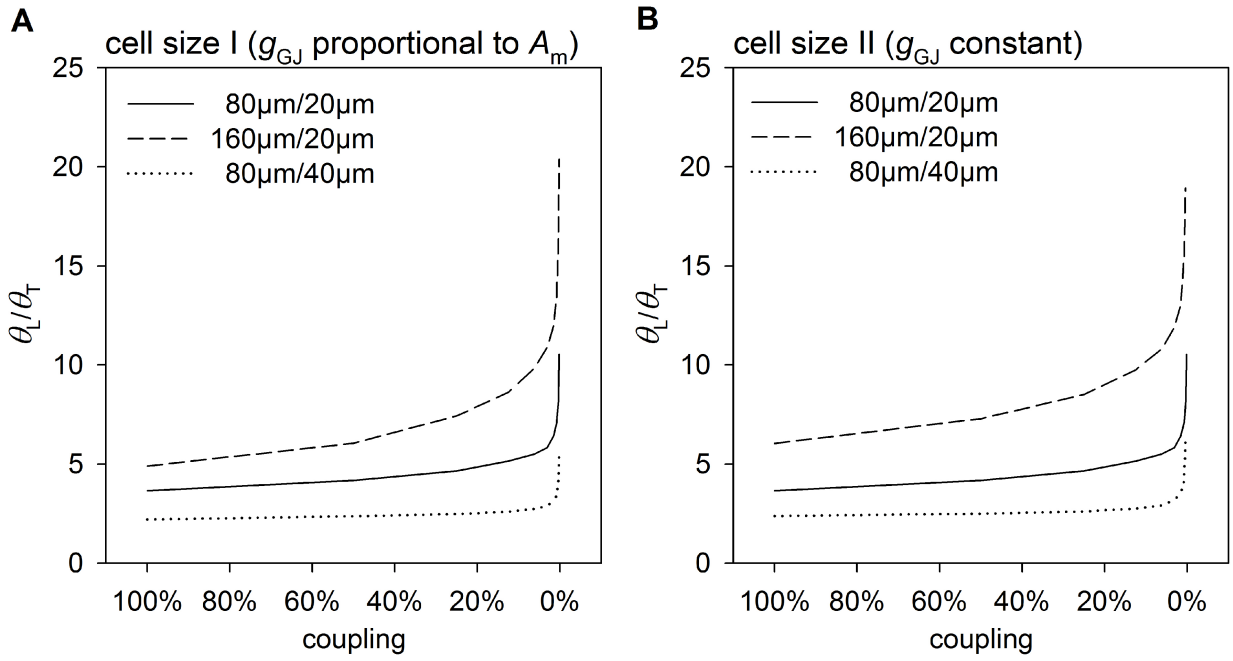

FIGURE S3 Effects of cell size on the ratio of longitudinal (θ_L) to transverse (θ_T) conduction velocity at different grades of junctional coupling. (*A*) Increased cell size assuming that gap junction conductance (g_{GJ}) per membrane area (A_m) remains constant, i.e., enlarged cells had greater g_{GJ}. (*B*) Increased cell size assuming constant g_{GJ}.

The θ_L/θ_T-ratio was strongly affected by the cell size and by the ratio of cell length to cell width. At 100% of coupling, θ_L/θ_T was ~3.6 in control cells, which had a ratio of length to width of 4. θ_L/θ_T was ~5 in long cells, which had a ratio of length to width of 8. θ_L/θ_T was ~2.2 in wide cells, which had a ratio of length to width of 2. Thus, the length-to-width ratio of a cell may be an approximation of the θ_L/θ_T-ratio. However, reducing intercellular coupling increased θ_L/θ_T slightly in the range between 100% and 20% of coupling, followed by a very fast increase if coupling was below 20%.

Figure S4

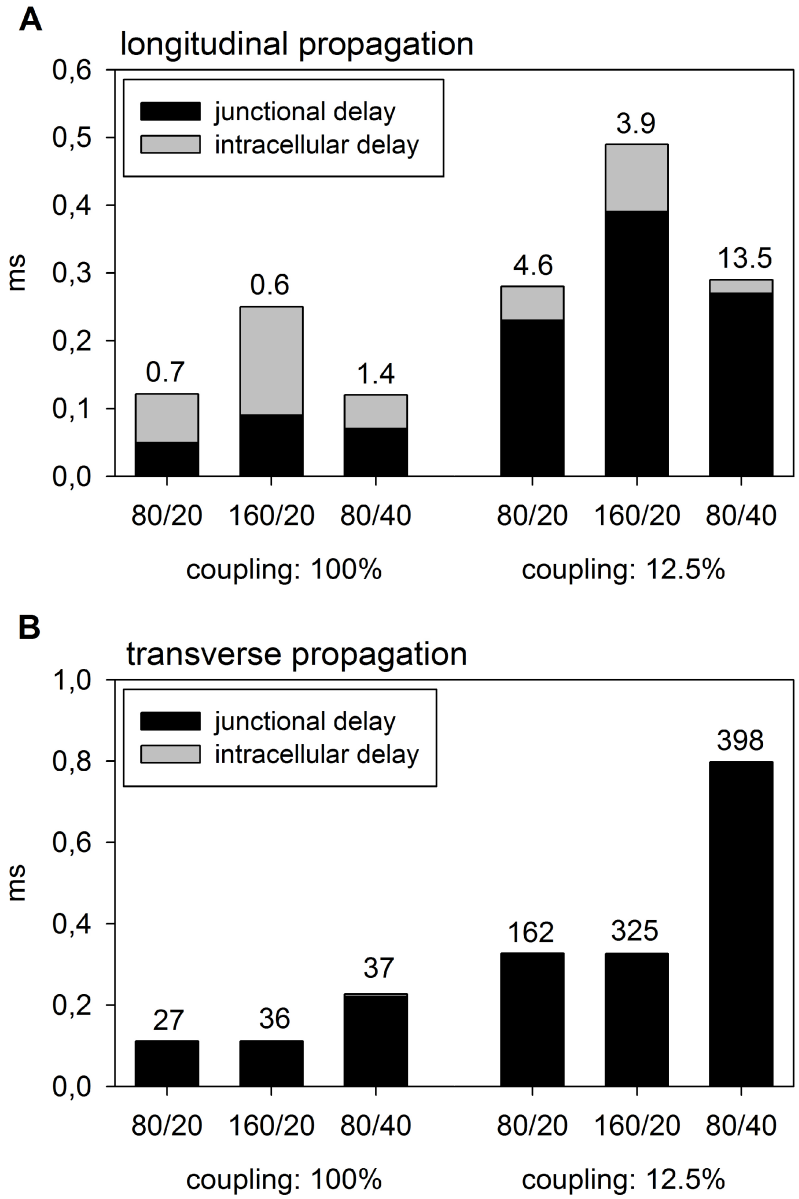

FIGURE S4 Junctional (*black*) and intracellular delays (*gray*) at 100% and 12.5% of coupling in control cells (length/width in μm: 80/20), long cells (160/20) and wide cells (80/40). g_{GJ} was adapted in enlarged cells to obtain the same conduction velocity at 100% of coupling as the control. Numbers above the bars indicate the ratio of junctional to intracellular delay. (*A*) Longitudinal propagation. (*B*) Transverse propagation.

A high ratio of junctional to intracellular delay indicates discontinuity. During longitudinal propagation (*A*), control cells and cells of increased length revealed similar values at high and low coupling: the ratio of junctional to intracellular delay was 0.7 and 0.6 at 100% of coupling and 4.6 and 3.9 at 12.5% of coupling, respectively. In contrast, wide cells showed significantly higher values: 1.4 at 100% of coupling and 13.5 at 12.5% of coupling, i.e., propagation in wide cells became earlier discontinuous. During transverse propagation (*B*), intracellular delay was already negligible at 100% of coupling, with very high ratios of junctional to intracellular delay (ranging between 27 and 37), indicating that in transverse direction there is always discontinuous propagation. This fits to the result that θ_T showed a similar decay during gradual uncoupling in all cell size groups and that θ_T is more affected by uncoupling than θ_L, leading to increased ratio of θ_L to θ_T at lower coupling.

Figure S5

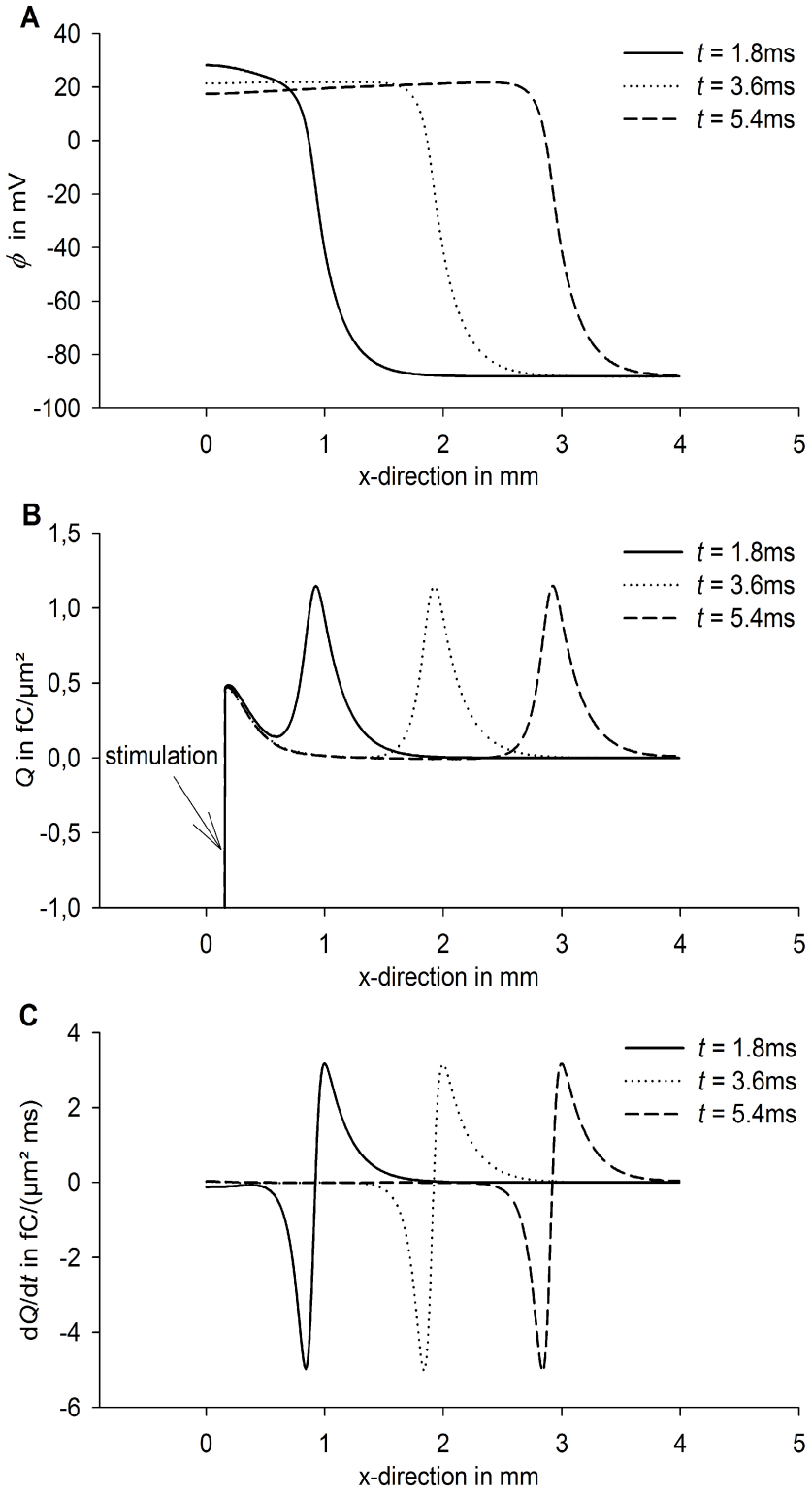

FIGURE S5 Impulse propagation in longitudinal direction under control conditions. Shown are membrane voltage (*A*), accumulated charge Q with respect to the tissue (*B*) and axial currents, i.e., $\mathrm{d}Q/\mathrm{d}t$ (*C*), at different points in time (t = 1.8ms, 3.6ms and 5.4ms). Note that *B* is the time integral of *C* over the period from t = 0ms until the point in time which is shown.

Each cell or cell segment accumulates charge from upstream cells until its activation (inflection points in *B*, points of zero-crossing in *C*). After its activation, it emits the same amount of charge to downstream cells ($\mathrm{d}Q/\mathrm{d}t < 0$), i.e., during stable AP propagation in planar waves the charge balance behind the wave front is zero. In elliptic waves, this is not the case. See also Figs. S6 and S7.

Figure S6

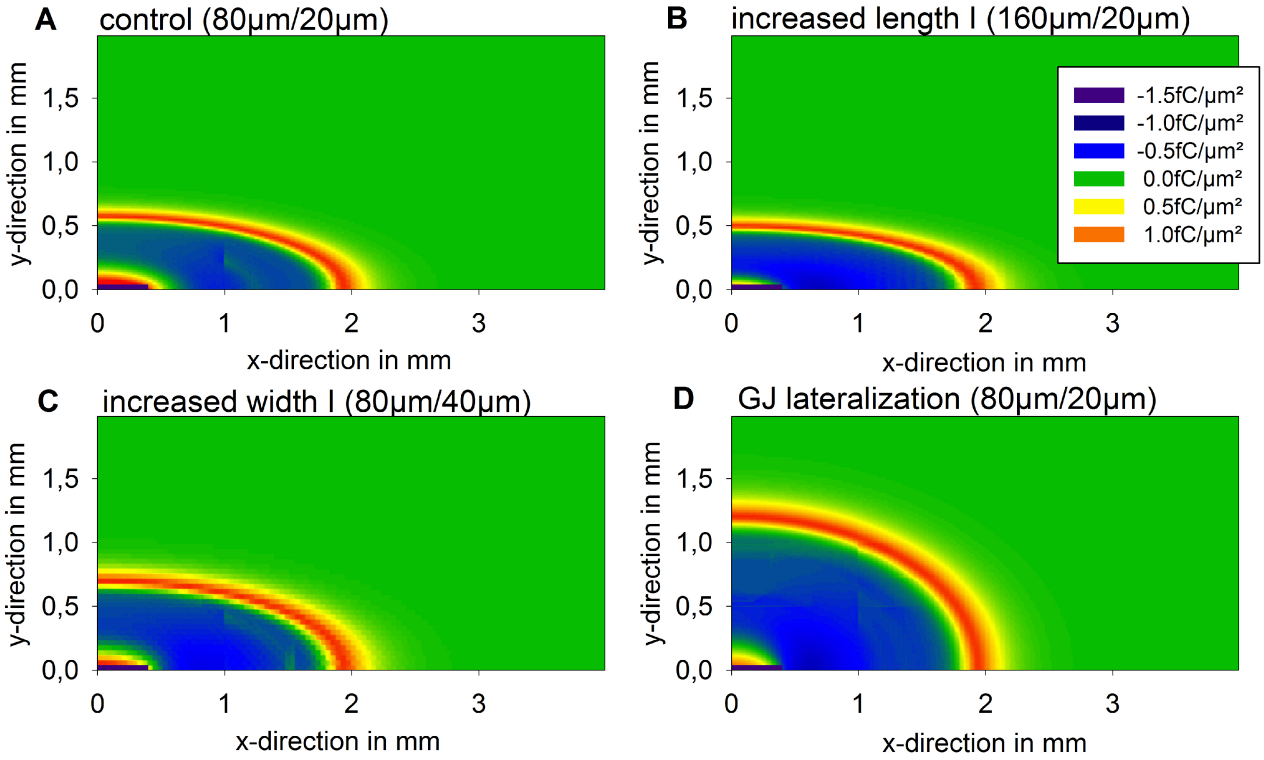

FIGURE S6 Elliptic wave propagation. Shown is the depolarizing charge (Q) in fC per µm² of membrane area which was accumulated (Q>0, current sinks) or emitted (Q<0, current sources) by each cell segment with respect to the tissue. Currents between segments and cells were integrated from t=0ms (time of stimulation) to the point in time at which the cell at (x,y)-position (2mm,0mm) was fully activated. Stimulation site was at position (0,0) causing the artifact. Control cells (*A*) were 80µm long, 20µm wide and had a lateral g_{GJ} of 2.6µS. Increased cell length (*B*) and increased cell width (*C*) were simulated with constant g_{GJ} per membrane area (assumption I). GJ lateralization (*D*) was simulated by a fivefold increase in lateral g_{GJ} from 2.6µS to 13µS.

Note that it is a general property of elliptic wave propagation that the charge balance behind the wave front is negative (*blue area*), i.e., cells emit more charge to the non-activated tissue than they accumulate before their own activation. This charge is gained from the extracellular space by depolarizing transmembrane currents (I_{Na}). The reason is that due to the curvature of the wave front there is an accelerated (non-constant) increase of activated tissue area per unit time. The area of current sink (yellow and red, Q>0) is increased in *C* and *D*, which is in accordance with the increased susceptibility to conduction block at tissue expansion, as shown in Figure 9 in the main article. Fig. S7 indicates the correlation between the stimulation current and charge accumulation by non-activated cells.

Figure S7

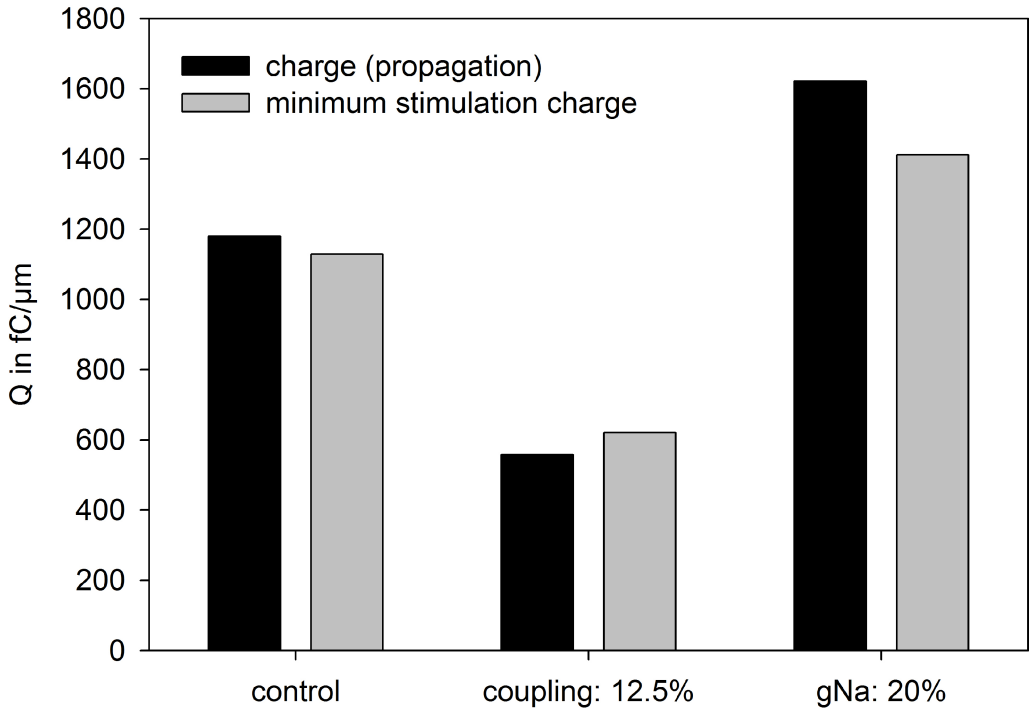

FIGURE S7 Correlation between the minimum stimulation charge (*gray*) which must be applied to the tissue in order to induce stable impulse propagation, and the total charge which is accumulated in front of the impulse wave during impulse propagation (*black*). Note that the charge indicated by the black bars corresponds to the area under the curve in Figure S5 *B*. The point in time is irrelevant because the curve does not change its shape or magnitude (Fig. S5 *B*). The unit fC/µm is the result of integrating over the tissue length. The stimulation charge Q_{stim} is calculated from the product of the stimulation current (I_{stim}, in pA per µm² of membrane area), the time interval of its application (t_{stim}), and the membrane area of its application (A_{stim}), with $A_{stim} = V_{stim} \times R_{AV}$. V_{stim} is the tissue volume which was stimulated, R_{AV} is the ratio of membrane area to tissue volume. For planar wave propagation, it is reasonable to normalize Q_{stim} to the tissue width and depth. Furthermore, different cell geometries can be compared by normalizing to R_{AV}. Thus, we get: $Q_{stim} = I_{stim} \times t_{stim} \times l_{stim}$. The minimum Q_{stim} was constant within a certain range of I_{stim}, t_{stim} and l_{stim} and only depended on the tissue properties. A minimum Q_{stim} of 1000fC/µm means that at least 1000fC must be applied to the stimulation site in tissue which has 1µm² of membrane area per 1µm of length (in the direction of planar wave propagation). The example shown here is for cells with a length/diameter of 80µm/20µm and for longitudinal propagation.

Note that minimum Q_{stim} and $Q_{propagation}$ are nearly equal, suggesting an analogy to the activation energy of a chemical reaction. While uncoupling reduced Q_{stim} and $Q_{propagation}$, a reduction of g_{Na} led to an increase, which is in good accordance with the findings during tissue expansion. High g_{GJ} and low g_{Na} increase the stimulation charge and, thus, the critical width of the source strand (Fig. 9 in the main article).

Figure S8

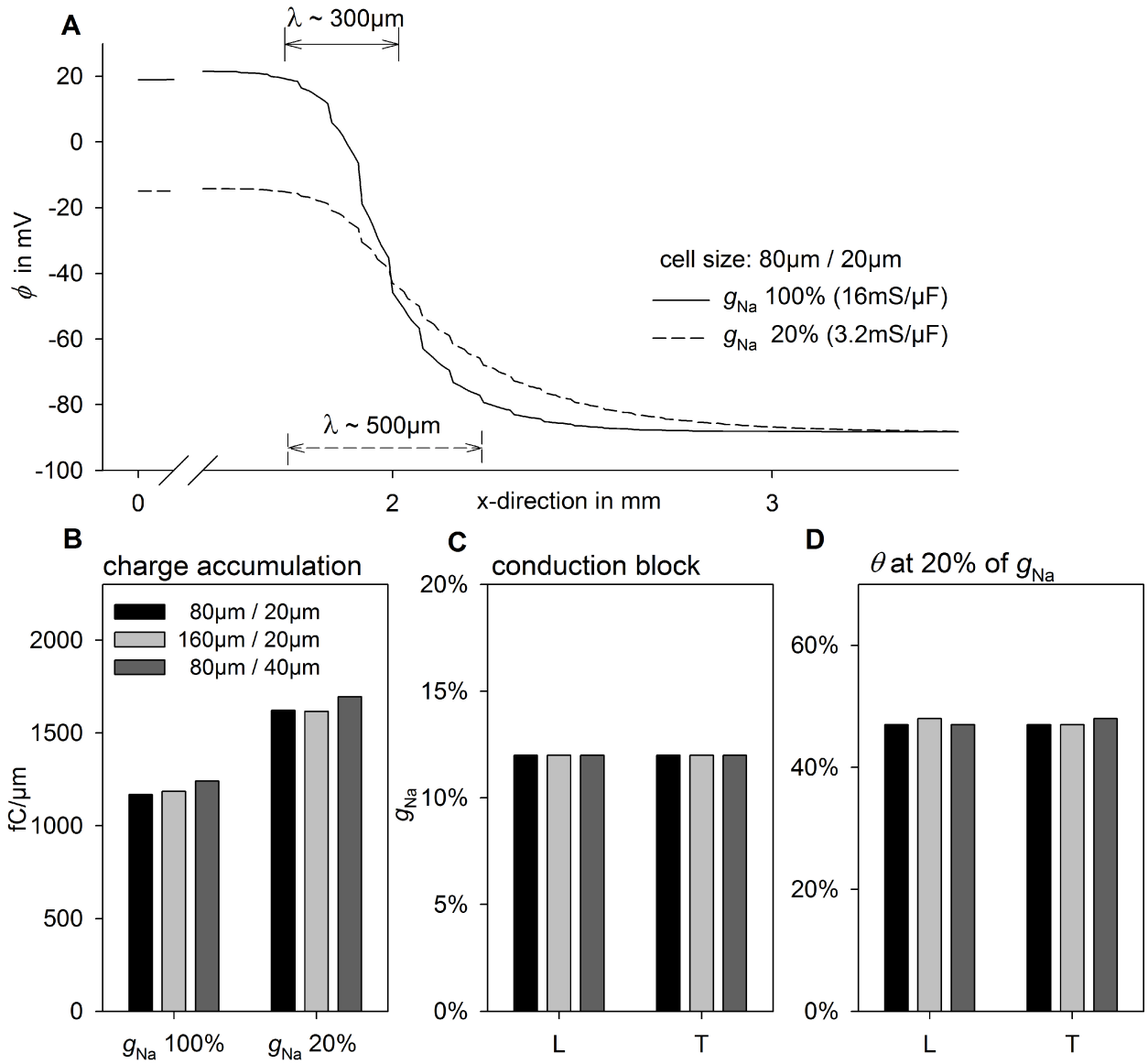

FIGURE S8 Effects of decreased maximum sodium channel conductance (g_{Na}) on different cell sizes. (*A*) Membrane potential (φ) in x-direction during longitudinal impulse propagation in control cells at 100% (16mS/µF) and 20% of g_{Na} (3.2mS/µF). Reducing g_{Na} increased the space constant (λ) and decreased maximum φ. (*B*) The charge which was accumulated by non-activated cells during longitudinal propagation in control cells (80µm/20µm), long cells (160µm/20µm) and wide cells (80µm/40µm) at 100% and 20% of g_{Na}. Note that this charge corresponds to the area under the curve in *A*, in the interval from the point where φ is approx. -40mV to x_{max}, multiplied by the specific membrane capacity (in pF/µm²) (*C*) Value of g_{Na} at which conduction block occurred during longitudinal (*L*) and transverse (*T*) impulse propagation. (*D*) Longitudinal (*L*) and transverse (*T*) conduction velocities (θ) at 20% of g_{Na}, normalized to their values at 100% of g_{Na}.

As a reduction of g_{Na} increases the space constant (*A*) , there is no different behavior of control cells, long cells or wide cells because impulse propagation remains continuous. As a result, the charge which was accumulated in front of activated cells was greater (*B*) at low g_{Na}. Conduction block occurred at 13% of g_{Na} in all groups (*C*) and a reduction of g_{Na} to 20% decreased longitudinal and transverse velocity uniformly to ~48% independently of the cell size (*D*).

REFERENCES

1. Dhein, S., and S. B. Hammerath. 2001. Aspects of the intercellular communication in aged hearts: effects of the gap junction uncoupler palmitoleic acid. *Naunyn Schmiedebergs Arch Pharmacol*. 364:397-408.
2. Jozwiak, J., and S. Dhein. 2008. Local effects and mechanisms of antiarrhythmic peptide AAP10 in acute regional myocardial ischemia: electrophysiological and molecular findings. *Naunyn Schmiedebergs Arch Pharmacol*. 378:459-470.
3. Polontchouk, L., J. A. Haefliger, B. Ebelt, T. Schaefer, D. Stuhlmann, U. Mehlhorn, F. Kuhn-Regnier, E. R. De Vivie, and S. Dhein. 2001. Effects of chronic atrial fibrillation on gap junction distribution in human and rat atria. *J Am Coll Cardiol*. 38:883-891.
4. Priebe, L., and D. J. Beuckelmann. 1998. Simulation Study of Cellular Electric Properties in Heart Failure. *Circ Res*. 82:1206-1223.
5. Luo, C. H., and Y. Rudy. 1994. A dynamic model of the cardiac ventricular action potential, I: simulations of ionic currents and concentration changes. *Circ Res*. 74:1071-1096.
6. Hodgkin, A. L., and A. F. Huxley. 1952. A quantitative description of membrane current and its application to conduction and excitation in nerve. *J Physiol*. 117:500-544.
7. Zhao, J., Y. Jin, L. Ma, and R. M. Corless. 2006. A highly efficient and accurate algorithm for solving the partial differential equations in cardiac tissue models. Proceedings of the International *Conference on Mathematical Biology*. 81-86.
8. Spach, M. S., and J. F. Heidlage. 1995. The stochastic nature of cardiac propagation at a microscopic level: an electrical description of myocardial architecture and its application to conduction. *Circ Res*. 76:366-380.
9. Shaw, R. M., and Y. Rudy. 1997. Ionic mechanisms of propagation in cardiac tissue. Roles of the sodium and L-type calcium currents during reduced excitability and decreased gap junction coupling. *Circ Res*. 81:727-741.
10. Botchway, A. N., M. A. Turner, D. J. Sheridan, N. A. Flores, and C. H. Fry. 2003. Electrophysiological effects accompanying regression of left ventricular hypertrophy. *Cardiovasc Res*. 60:510-517.
11. Cascio, W. E., G. X. Yan, and A. G. Kleber. 1990. Passive electrical properties, mechanical activity, and extracellular potassium in arterially perfused and ischemic rabbit ventricular muscle. Effects of calcium entry blockade or hypocalcemia. *Circ Res*. 66:1461-1473.
12. Yao, J. A., W. Hussain, P. Patel, N. S. Peters, P. A. Boyde, and A. L. Wit. 2003. Remodeling of gap junctional channel function in epicardial border zone of healing canine infarcts. *Circ Res*. 92:437-43.
13. Yao, J.A., D. E. Gutstein, F. Liu, G. I. Fishman, and A. L. Wit. 2003. Cell coupling between ventricular myocyte pairs from connexin43-deficient murine hearts. *Circ Res*. 93:736-43.
14. Kleber, A. G., M. J. Janse, F. J. Wilms-Schopmann, A. A. Wilde, and R. Coronel. 1986. Changes in conduction velocity during acute ischemia in ventricular myocardium of the isolated porcine heart. *Circulation*. 73:189-198.
15. McIntyre, H., and C. H. Fry. 1997. Abnormal action potential conduction in isolated human hypertrophied left ventricular myocardium. *J Cardiovasc Electrophysiol.* 8:887-894.
16. Weingart, R., and P. Maurer. 1988. Action potential transfer in cell pairs isolated from adult rat and guinea pig ventricles. *Circ Res*. 63:72-80.
17. Hagen, A., A. Dietze, and S. Dhein. 2009. Human cardiac gap-junction coupling: effects of antiarrhythmic peptide AAP10. *Cardiovasc Res*. 83:405-415.
18. Müller, A., T. Schaefer, W. Linke, T. Tudyka, M. Gottwald, W. Klaus, and S. Dhein. 1997. Actions of the antiarrhythmic peptide AAP10 on intercellular coupling. *Naunyn Schmiedebergs Arch Pharmacol*. 356:76-82.
19. Hubbard, M. L., W. Ying, and C. S. Henriquez. 2007. Effect of gap junction distribution on impulse propagation in a monolayer of myocytes: a model study. *Europace*. 9:vi20-vi28.
20. De Bakker, J. M., F. J. Van Capelle, M. J. Janse, S. Tasseron, J. T. Vermeulen, N. De Jonge, and

J. R. Lahpor. 1993. Slow conduction in the infarcted human heart. 'Zigzag' course of activation. *Circulation*. 88:915-926.

21. Benitah, J. P., J. L. Alvarez, and A. M. Gómez. 2010. L-type Ca(2+) current in ventricular cardiomyocytes. *J Mol Cell Cardiol*. 48:26-36.
22. Sakakibara, Y., T. Furukawa, D. H. Singer, H. Jia, C. L. Backer, C. E. Arentzen, and J. A. Wasserstrom. 1993. Sodium current in isolated human ventricular myocytes. *Am J Physiol*. 265:H1301-1309.
23. Chorvatova A, Snowdon R, Hart G, Hussain M. 2004. Effects of pressure overload-induced hypertrophy on TTX-sensitive inward currents in guinea pig left ventricle. *Mol Cell Biochem*. 261:217-226.
24. Rojas Gomez, D. M., J. S. Schulte, F. W. Mohr, and S. Dhein. 2008. Alpha-1-adrenoceptor subtype selective regulation of connexin 43 expression in rat cardiomyocytes. *Naunyn Schmiedebergs Arch Pharmacol.* 377:77-85.
25. Fast, V. G., and A. G. Kléber. 1995. Block of impulse propagation at an abrupt tissue expansion: evaluation of the critical strand diameter in 2- and 3-dimensional computer models. *Cardiovasc Res*. 30:449–459.
26. Cabo, C., and P. A. Boyden. 2009. Extracellular space attenuates the effect of gap junctional remodeling on wave propagation: a computational study. *Biophys J*. 96:3092-3101.